

Optimizing quantum control pulses with complex constraints and few variables through Tensorflow

Yao Song,¹ Junning Li,² Yong-Ju Hai,^{1,3} Qihao Guo,¹ and Xiu-Hao Deng^{1,4,*}

¹*Shenzhen Institute of Quantum Science and Engineering,
Southern University of Science and Technology, Shenzhen, Guangdong 518055, China*

²*Department of Physics, City University of Hong Kong,
Tat Chee Avenue, Kowloon, Hong Kong SAR, China*

³*Department of Physics, Southern University of Science and Technology, Shenzhen 518055, China*

⁴*Guangdong Provincial Key Laboratory of Quantum Science and Engineering
Southern University of Science and Technology, Shenzhen, Guangdong 518055, China*

Applying optimal control algorithms on realistic quantum systems confronts two key challenges: to efficiently adopt physical constraints in the optimization and to minimize the variables for the convenience of experimental tune-ups. In order to resolve these issues, we propose a novel algorithm by incorporating multiple constraints into the gradient optimization over piece-wise pulse constant values, which are transformed to contained numbers of the finite Fourier basis for bandwidth control. Such complex constraints and variable transformation involved in the optimization introduce extreme difficulty in calculating gradients. We resolve this issue efficiently utilizing auto-differentiation on Tensorflow. We test our algorithm by finding smooth control pulses to implement single-qubit and two-qubit gates for superconducting transmon qubits with always-on interaction, which remains a challenge of quantum control in various qubit systems. Our algorithm provides a promising optimal quantum control approach that is friendly to complex and optional physical constraints.

I. INTRODUCTION

Potential ground-breaking quantum technologies, such as quantum computing, quantum sensing, and quantum metrology [1–3], become more and more feasible with the tremendous progress of quantum control technology on various physical systems [4–7]. Based on growing knowledge quantum systems interacting with the environment, multifarious approaches have been developed to improve the control precision [8–14]. Eventhough, further optimizing quantum control still highly relies on numerical approaches [14–19]. Practical quantum optimal control (QOC) [20–23] should satisfy the requirements and constraints in the physical systems, such as more realistic Hamiltonian, maximal field strength, finite sampling rate, limited bandwidth [24–26], etc. Also, for efficient calibration in experiments, the control field waveform should depend on as few variables as possible. Other than the physical considerations, the optimization algorithm ought to be fast and accurate and should be extensible to larger systems. As one of the most successful numerical optimization algorithms, GRAPE has been applied to many physical systems, including NMR qubits [15, 27–30], superconducting qubits in 3D cavity [31–35], nitrogen-vacancy (NV) centers in diamond [6, 36–38], etc. However, adapting GRAPE to multiple realistic constraints remains challenging. Different from GRAPE, another numerical algorithm, CRAB has been proposed to generate smooth control waveforms, towards application in cold atoms [39]. There are also many

other proposed algorithms leading to promising applications [17, 18, 40, 41]

Depending on how to parametrize the control field's variables, QOC algorithms could be assorted into two classes: 1. *Piecewise constant* (PWC) discretizes the field pulse as a sequence of piecewise-constant field strength and the value of each piece as the optimization variable [15, 16, 42–44]. Varying each variable causing local variation of the whole waveform hence local variation of the expectation function, which preserves the convexity of optimization landscape in this parameter space. And then gradient-based optimization could efficiently proceed [15, 17, 18, 42]. A trade-off arises between inaccurate PWC dynamics for finite discretization rate and the cost of computing the gradients versus massive variables. Also, PWC waveforms are not smooth and could easily contain fast fluctuations. Filtering the optimized waveform in the post-optimization deforms the output pulses from optimum. 2. *Chopped basis* (CB) optimization uses parameters related to a finite set of basis expanding the control waveform. The basis are usually analytic functions such as Gaussian, tangential, or Fourier functions [14, 19], etc, which easily guarantees the smoothness of the optimized waveform. However, adding the physical constraints deforms the processed pulses in an unknown way [14, 19], so the output pulses lose the analyticity. Furthermore, small change of one expansion coefficient leads to global deformation of the pulse waveform, and also coefficients of different bases affect differently. Therefore, the CB optimization landscape becomes non-convex. Alternatively, constraints could be incorporated into optimization with Lagrange multipliers but the calculation of the analytical differentiation brings in another source of complexity and difficulty [41, 45, 46].

*Electronic address: dengxh@sustech.edu.cn

Here in this article, we propose a novel optimization algorithm, the *Complex and Optional Constraints Optimization with Auto-differentiation* (COCOA), to tackle the problems summarized above. The algorithm parametrizes the control waveform in the basis of truncated Fourier series, while the optimization performs the gradient in the convex landscape of PWC parameter space. The transformation between the aforementioned two parametrization systems is bridged via approximate discrete Fourier transformation (DFT) and inverse discrete Fourier transformation (iDFT). The advantage of combining these two parametrization systems is that all the pulse constraints can be incorporated in the optimization process instead of post-optimization. The application of DFT and iDFT within the optimization iteration introduces further physical advantages: 1. Hard bounds on the bandwidth by limiting the Fourier basis; 2. Definite expansion with pre-selected basis; 3. Analytical expression of output pulses with a small number of parameters for tuning. 4. Convenient application of pulse pre-distortion because the transfer/filter functions are in the frequency domain[26, 47, 48]. However, embedding these constraints and the transformation of parametrization systems into the optimization iteration raises extreme difficulty in solving the analytical gradient equations. We resolve this issue using auto-differentiation during one-round back-propagation process provided by Tensorflow[49]. With Tensorflow, the automatical calculation of gradient could be further extended to various physical systems. This paper explains in detail how COCOA works and presents some numerical results to demonstrate the efficiency and its advantage compared with GRAPE and CRAB.

This paper is organised as follows. First, we take an overview of quantum optimal control theories and numerical methods. In Sec. III we present the algorithmic description of COCOA and explain how it combines the advantages of two categories QOC approaches and perform an optimization task under complex and optional constraints. Then in Sec. IV, we apply COCOA to find optimal quantum-gate pulses for superconducting qubits with always-on interactions. We simulate two models: cavity mediated two-qubit system and direct capacitively-coupled systems. We demonstrate COCOA's advantages by comparing with the representative algorithms GRAPE and CRAB of the two QOC categories. In Sec. V, we conclude this paper.

II. QUANTUM OPTIMAL CONTROL

A. General formalism

We consider a general Hamiltonian in QOC problem as

$$H(t) = H_d + H_c(t) \quad (1)$$

where H_d is the drift Hamiltonian of the system. $H_c(t)$ is the time-dependent Hamiltonian which is to be optimized to control the quantum system to undergo a desired time evolution. The dynamics of the system steered by the total Hamiltonian in Eq. (1) satisfied the Schrödinger equation $|\dot{\psi}(t)\rangle = -iH(t)|\psi(t)\rangle$, with the time evolution operator satisfying $\dot{U}(t) = -iH(t)U(t)$, or an integral form $U(t) = \mathcal{T}e^{-i\int H(t)dt}$, where \mathcal{T} is the time-ordering operator. A generic form of the control Hamiltonian is $H_c(t) = H_c(\{\Omega_j(t)\}, t)$, where $\{\Omega_j(t)\}$ are a set of time-dependent control pulse to be optimized. In our examples presented later, $\{\Omega_j(t)\}$ are chosen to be the envelopes of microwave drives on qubits, where $j = 1x, 1y, 2x, 2y$, i.e. $1x$ means rotating around X axis for qubit 1. For different QOC problems, expectation function could be customized. A constrained optimization could be performed by combining penalty functions into the expectation function with Lagrange multipliers [45, 50]. In the specific examples discussed in this article, we study the performance of a quantum gate at final time $t = T$ as an average over all possible initial quantum states. It can be quantified by the average gate fidelity [51] defined as

$$f = \frac{1}{d(d+1)}(\text{Tr}(MM^\dagger) + |\text{Tr}(M)|^2) \quad (2)$$

where $M = U_{tar}U_T$, d is the dimension of the quantum system. Therefore, we use infidelity as the cost function to be minimized, i.e. $F = 1 - f$.

B. Realistic requirements

Traditional pulse optimization algorithms are confronted with many issues while applying to realistic systems. We summarize various realistic issues below and design the COCOA optimization to bridge the gap between numerical optimization and experimental applications.

1. *Pulse pre-distortion.* Pulse distortion as one of the major issues could take place in the following process [52]: i) Pulse generation with finite sampling rates, which could be modeled as FIR filter. ii) Transmission of signal, where a IIR transfer function could be used to model the distortion. iii) Numerical distortion when post-processing the optimal pulse for the purposes such as smoothing, which could be modelled as the post-optimization filter function. Commonly, the processed pulse is not optimal any more. Pulse pre-distortion with inverse filter function could be applied in experiments to compensate these effects[26, 53]. Since the filter functions are in frequency domain, it would be much more convenient for pre-distortion if the numerical output pulse is an analytical function for frequency rather than in the PWC form.

2. *Pulse constraints:* Optimal pulses should satisfy various physical constraints, such as smoothness, finite bandwidth, bounded amplitude, starting and ending at

some designated values, robustness to some randomness (e.g. noises), and so on. Post-processing the optimized pulses with constraints results in numerical pulse distortion mentioned above. So it is necessary to incorporate constraints into the optimization. However, efficiently adding pulse constraints to the optimization is challenging, because the gradient might be too complicated to compute. Traditionally, conditional expressions such as if-else paragraph could be added into the optimization solver. But this results in possible loopholes and low efficiency. So a better approach is still open for investigation.

3. *Pulse parameters.* Optimizing the pulse parameters in experiments is necessary and could become exponentially strenuous when the number of parameters grows. Therefore, it is desired to obtain optimal pulses with few parameters for experimental tune-ups.

4. *Analyticity of the pulse.* The analyticity is defined as explicit and analytical function or a definite summation of several analytical functions, which helps generating and tuning control pulses in experiments.

In this article, we will show how the COCOA algorithm is engineered to satisfy the above requirements efficiently. And we will test its performance via realistic optimization tasks.

III. COCOA ALGORITHM

A. List of symbols

Symbol	Meaning
j	Index of control pulse ($1x, 1y, 2x, 2y$)
k	Time slice index ($1, \dots, N$)
$\Omega[k]$	Control amplitude in time slice k
$\mathcal{C}, \mathcal{M}, \mathcal{E}, \mathcal{F}$	Transform function for each node: pulse constraint, bandwidth control, evolution, cost function
$\Omega^r(t)$	Control pulse at iteration r
N_c	Number of Fourier components kept in optimized pulse
R	Number of iterations in optimization
α	Learning rate
ϵ_0	Tolerance of cost function
ϵ_1	Tolerance of gradient norm
T	Total gate time
S_0	Initial state
S_T	State at time $t = T$
U_T	Evolution operator at time $t = T$
U_{tar}	Target operator
$\Omega_j^*(t)$	Optimized pulse of j -th control

B. Pseudo code

The pseudo code of COCOA algorithm can be seen in Algorithm 1.

Algorithm 1 Complex and Optional Constraints Optimization (COCO) for pulse engineering

Require: cost function: F ; initial pulse sequence: $\Omega_j^0(t)$; N_c ; α ; Iterations: R ; ϵ_0 ; ϵ_1
Ensure: optimized pulse: $\Omega_j^*(t)$
1: Discretization: $\Omega_j^0(t) \rightarrow \{\Omega_j^0[k]\}$;
2: **repeat**
3: record computational graph for auto-differentiation;
4: pulse constrain: $\{\Omega_j[k]\} \rightarrow \{\tilde{\Omega}_j[k]\}$;
5: bandwidth control: $\{\tilde{\Omega}_j[k]\} \rightarrow \{\hat{\Omega}_j[k]\}$;
6: evolution: $U_k = e^{-i\left(H_d + \sum_j \hat{\Omega}_j[k] H_j[t_k]\right)\Delta t}$, $U_T = U_N U_{N-1} \dots U_1$;
7: cost function: $F(U_T, S_T)$;
8: calculate gradient using auto-differentiation: $\left\{\frac{\partial f}{\partial \Omega_j[k]}\right\}$;
9: **until** $(F(U_T, S_T) < \epsilon_0$ or $\|\frac{\partial f}{\partial \{\Omega_j[k]\}}\| < \epsilon_1)$;

C. Algorithm settings

The process of COCOA is shown as a flowchart in Fig. 1. The four main nodes in COCOA are pulse constraint, bandwidth control, evolution, and cost function. Pulse constraints and bandwidth control node are the core nodes, which always do a pretreatment on the pulse before evolution, while the form of evolution node and cost function node depend on the problem and optimization task. In the following, we elaborate each node and illustrate several unique features of CRAB.

1. Ansatz for pulses

The initial guess in COCOA can be chosen to be either a random guess or a specific form based on prior knowledge. Then it is transformed to an function for pulse parameters $\Omega_j(\vec{p}, t)$, where \vec{p} is the parameter vector. The analytical form of this function could be arbitrary according to the need in practice. For the consideration of limiting pulse bandwidth, without loss of generality, we take chopped Fourier basis functions as

$$\Omega_j(\vec{p}, t) = a_0 + \sum_{n=1}^{N_c} A_{jn} \cos(\omega_{jn}t) + B_{jn} \sin(\omega_{jn}t), \quad (3)$$

where pulse parameter set \vec{p} is formed with Fourier expansion parameters

$$\vec{p} = \{A_{jn}, B_{jn}, a_0\}. \quad (4)$$

Analytical pulse functions solved from different theories could be exactly or approximately transformed to the

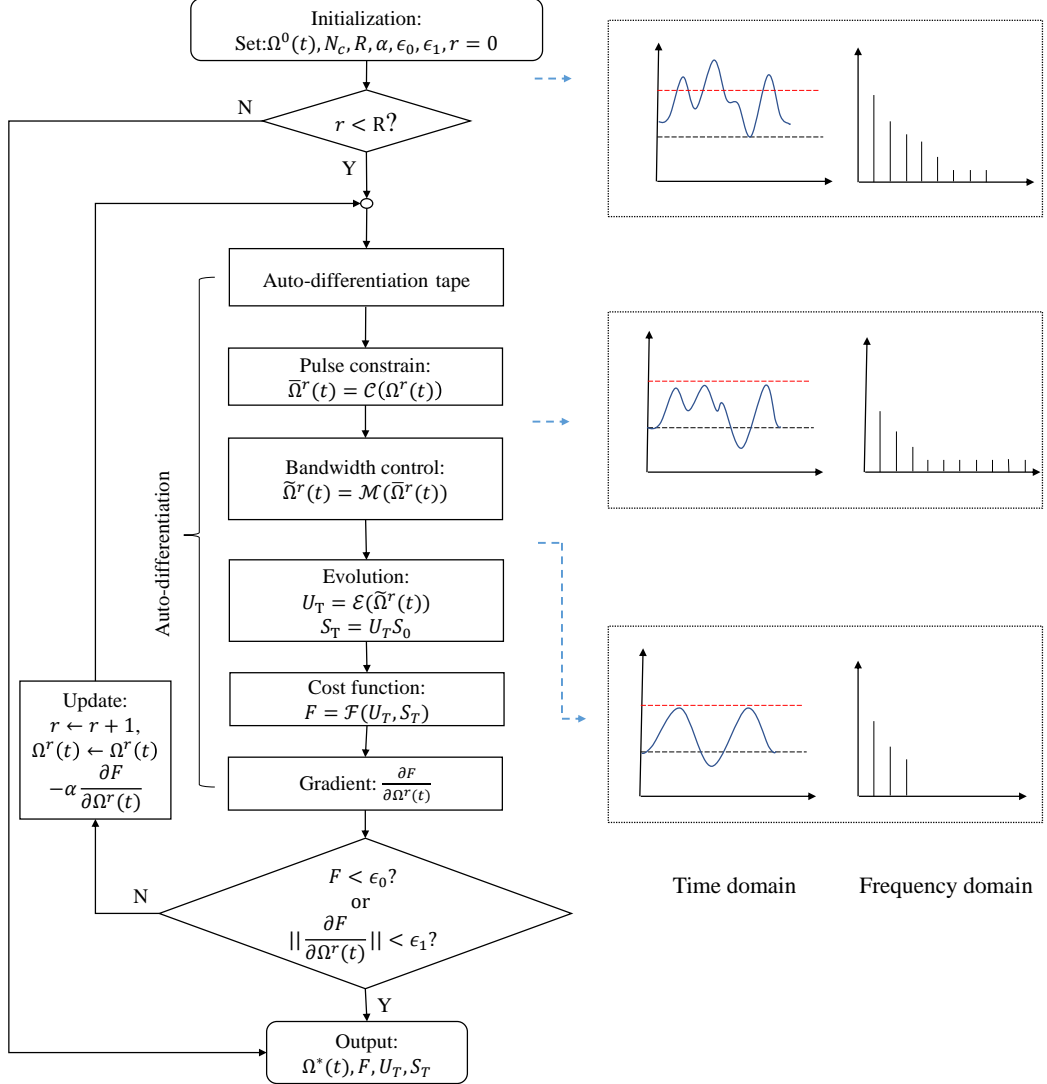


FIG. 1: Flow diagram of COCOA. We use transform functions $\mathcal{C}, \mathcal{M}, \mathcal{E}, \mathcal{F}$ to denote the 4 main nodes. Auto-differentiation tape is just a recorder that records all the computing processes automatically by Tensorflow and will be used for computing gradient. The figures on the left show the pulse's change in time and frequency domain after each specific node.

chopped Fourier basis for optimization, such as Slepian pulses [54], SWIPHT pulses [9, 10], geometric pulses [12], and so on. We will demonstrate this in Sec.IV B 1. Note that filter functions for pulse pre-distortion could be directly applied on the Fourier basis, which brings additional convenience to experimental tune-ups.

In the PWC optimization, $\Omega_j(\vec{p}, t)$ is discretized to a N -length sequence with sampling frequency $f_s = N/T$, where T is the total gate time.

$$\Omega_j(\vec{p}, t) \xrightarrow{\text{sample}} \{\Omega_j[\vec{p}, k]\}, k = 1, \dots, N. \quad (5)$$

For convenience, the discretized temporal sequence of the PWC ansatz is denoted as $\{\Omega_j[k]\}, k = 1, \dots, N$.

2. Amplitude constraint

A realistic system limits a maximal strength of the control field. Also, a single control pulse starts and ends at zero. As a traditional way in textbook [15, 55], this constraint enters the optimization cost function by adding up with the control power defined as $J = \lambda \int_0^T \Omega_j^2(t) dt$, where the weight $\lambda > 0$. However, the fidelity of optimized pulse will be lower with this term added. Furthermore, this way just gives a soft constraint on amplitude maximum, which could be harmful when physical systems have a hard limit on control amplitude. In our algorithm, a strong constraint to the pulse amplitude is added by passing the control pulses through a sigmoid

window function, similar to GOAT [14].

$$S_{down}(t, g) = \frac{1}{1 + e^{gt}} \quad (6)$$

$$S_{up}(t, g) = 1 - S_{down}(t, g) \quad (7)$$

$$S_{amp}(\Omega_j[k], l, u) = \left(2S_{up} \left(\frac{\Omega_j[k] - \frac{u+l}{2}}{\frac{u-l}{2}}, 0.5 \right) - 1 \right) \frac{u-l}{2} + \frac{u+l}{2}, \quad (8)$$

where g is the ascent/descent gradient of the window function. l, u are the lower and upper bound of the pulse's amplitude.

The total amplitude constraint transformation reads

$$\begin{aligned} \mathcal{C}(\Omega_j[k], t, l, u, g, \Delta t) \\ = S_{up} \left(\frac{t - \Delta t}{T}, g \right) S_{down} \left(\frac{t - (T - \Delta t)}{T}, g \right) S_{amp}(\Omega_j[k], l, u), \end{aligned} \quad (9)$$

where Δt is the width of the ascent(descent) edge. The first and the second sigmoid function ensures zero amplitude at $t = 0$ and $t = T$, and thus satisfies the second physical constraint. The last one bounds the amplitude to the $[l, u]$ range.

3. Bandwidth control

In this node, We modulate the control pulse to a bandwidth-limited one in frequency domain. Firstly, we transform the pulse sequence from time domain into frequency domain using discrete Fourier transform (DFT)

$$X[n] = \sum_{k=1}^N \Omega_j[k] e^{i(2\pi n/N)k}. \quad (10)$$

After DFT, We get a complex sequence $\{X[n]\}, n = 1, \dots, N$. Assuming the upper cut-off frequency is f_{th} , we can derive the maximal Fourier component number N_c

$$N_c \leq \text{Int} \left(N \frac{f_{th}}{f_s} \right) \quad (11)$$

where $\text{Int}(\cdot)$ indicates rounding down. Here, N_c is a hyper-parameter in our algorithm and it affects the pulse's simplicity, smoothness and numerical accuracy. We will discuss it in details in Sec. IV.

After DFT, the higher Fourier components over N_c , namely the complex sequence elements from $X[N_c + 1]$ to $X[N - N_c]$ will be set to zero, i.e. limiting the bandwidth. Then the complex sequence in frequency domain becomes

$$Y[n] = \begin{cases} \tilde{X}[n], & n \in [1, N_c] \cup [N - N_c, N] \\ 0, & n \in [N_c + 1, N - N_c] \end{cases} \quad (12)$$

Then we apply the inverse transformation of DFT, called IDFT, to transform the pulse back to time domain

$$\tilde{\Omega}_j[k] = \frac{1}{N} \sum_{n=1}^N Y[n] e^{i(2\pi k/N)n}. \quad (13)$$

After IDFT, the pulse sequence $\{\tilde{\Omega}_j[t_k]\}$ is a smooth pulse sequence with limited bandwidth. Its functional form in continuous time domain is denoted as

$$\tilde{\Omega}_j(t) = a_0 + \sum_{n=1}^{N_c} A_n \cos \left(n \frac{2\pi f_s}{N} t + \phi_n \right). \quad (14)$$

It is worth noting that this is the functional form of our final optimized waveform, which is a finite Fourier basis function. More details about DFT and IDFT can be seen in appendix A.

4. Evolution

For the evolution node, the smooth, analytical and bandwidth-limited control pulse, Eq. (14), obtained from the previous nodes is taken into the dynamical equation to compute the time evolution. The choice of evolution equations, such as master equation and Schrödinger equation, depends on the specific physical problem and optimization task. Here we consider a closed quantum system and use the PWC approach for the time evolution. Note that this could be upgraded to other finite difference methods to obtain more precise solution of the Schrödinger equation. Here, the evolution operator at time t_k reads

$$\begin{aligned} U_k &= e^{-iH[t_k]\Delta t} \\ &= e^{-i \left(H_d + \sum_j \tilde{\Omega}_j[t_k] H_j[t_k] \right) \Delta t}. \end{aligned} \quad (15)$$

Then final evolution operator at time $t = T$ reads

$$U_T = U_N \dots U_1 U_0. \quad (16)$$

The final state S_T reads

$$S_T = U_T S_0. \quad (17)$$

D. Pulse distortion in numerical process

There are at least three steps of pulse distortion in a complete quantum control task. First, the pulse distorted from the waveform optimized numerically because of the finite sampling rate of the arbitrary waveform generator (AWG) [56, 57]. Second, the pulse experience distortion during the transmission due to impedance mismatching and other realistic filtering effects [25, 26, 53, 58]. Third, to force the optimized pulses satisfy physical constrains, pulse distortion is often induced when post-processing

the output pulses from optimization iteration, such as adding filter functions to the output. As mentioned above, PWC algorithms, such as GRAPE and Krotov, generates rough pulses. In order to smoothen the optimal pulses, low-pass filter such as Gaussian filter [59] could be applied to suppress or cut off the high frequency components and limit the bandwidth, after which the resultant waveform deforms and the fidelity is lowered from the optimum. On the other hand, limiting pulse amplitude [14] by applying a constraint function to the optimization results in distortion from the analytical form and induces additional high frequency components. However, COCOA introduce all the pulse constraints into the optimization before the DFT node and all the high frequency component will be filtered, overcoming this kind of pulse distortion perfectly. Additionally-customized constraints could be incorporated as well. This is enabled with the use of auto-differentiation in Tensorflow, which is discussed next. As a result, the optimized pulse is band-limited, maximum-limited, starting/ending at ZERO while a definite analytical waveform is guaranteed to output from the algorithm. This will be illustrated in Sec. IV

E. Auto-differentiation

Auto-differentiation (AD) method is widely used in machine learning, which is almost as accurate as symbolic differentiation [60]. There are two points of necessity that we choose AD: (1) AD obtains the derivatives to all inputs in one back-propagation when AD works in the reverse mode. So it is much more efficient than manual and symbolic differentiation, and is more precise than numerical differentiation. (2) The complexity of derivatives induced by the bandwidth control and the extraction of computational subspace places much difficulties, such as expression swell problem, to manual and symbolic differentiation. The feasibility of auto-differentiation is demonstrated by the fact that each node of COCOA is derivable theoretically, so as the total transform function of inputs to cost function is $\mathbb{F} : \mathbb{R}^n \rightarrow \mathbb{R}$. This is suitable for the reverse mode of AD because the dimension of inputs is larger than outputs. We explicitly elaborate the process of auto-differentiation in COCOA optimization in Fig. 2. There are two processes when using auto-differentiation in reverse mode. i) Forward-propagation: when computing from $\{\Omega_j[k]\}, k = 1, \dots, N$ to F , it automatically constructs a computational graph formed of nodes and edges, as shown in Fig. 2 (solid line). ii) Back-propagation: The gradients of F versus all inputs $\{\Omega_j[k]\}, k = 1, \dots, N$ are calculated with the computational graph by using chain rule, as shown in Fig. 2 (dashed line). We note that all the derivatives of F with respect to inputs $\{\Omega_j[k]\}, k = 1, \dots, N$ are calculated in one back-propagation, which makes AD more efficient than other methods. Our numerical simulation results in Sec. IV will demonstrate the AD's efficiency in

quantum optimal control. For more details of AD, please refer to [60].

IV. APPLICATIONS ON SUPERCONDUCTING QUBITS

To demonstrate the advantage of COCOA, we apply this algorithm to tackle one of the most challenging control obstacles in the up-to-date multi-qubit processors: the always-on couplings. Such issue lies in many qubit systems such as superconducting qubits [12, 61, 62], quantum dots [63–65], NMR qubits [66, 67], etc. Scaling-up qubit systems tends to reduce the number of control degrees, which means taking out more control fields out of the system. Losing either the control of qubit frequencies or coupling strength brings more difficult in realizing good quantum gates, especially in the systems such as fixed frequency qubits with fixed couplings, tunable qubits with residual couplings, qubits with tunable couplings with unwanted interaction and crosstalk [68–70]. Fortunately, the degree of control freedom on the pulse-shaping could be further exploited with the help of COCOA. In this section, without loss of generality, we consider two realistic models of multi-connected superconducting qubits and apply COCOA to find optimal control pulses for single-qubit and two-qubit gates for the always-coupled qubits.

A. Model 1: Two transmon qubits coupled directly

In X-mon (X-shaped transmon) arrays where qubits are coupled directly via a capacitance with a constant interaction g , such as Google's previous version of quantum computing chip Bristlecone [71] and other chip design with few control lines [13]. As a simplified model, we consider two qubit coupled directly and obtain the Hamiltonian as

$$H_0 = \sum_{j=1,2} \omega_j a_j^\dagger a_j + \frac{\alpha_j}{2} a_j^\dagger a_j^\dagger a_j a_j + g_{12} (a_1^\dagger + a_1)(a_2^\dagger + a_2) \quad (18)$$

This model is effectively valid for qubits coupled via tunable couplers [12, 72]. Here ω_j are the qubit frequencies and α_j are the anharmonicities of transmon qubits, $j = 1, 2$. To implement single qubit operations, neighbour qubits are detuned with $\Delta = \omega_1 - \omega_2$ and the effective zz -coupling strength is turned down with the rate $\frac{g_{12}^2}{\Delta}$ [12, 73–75]. g_{12} is the capacitive coupling strength between two qubits. $a^\dagger(a)$ denotes the qubit creation (annihilation) operators. This unwanted coupling gives rise to frequency splitting between $|00\rangle \rightarrow |01\rangle$ and $|10\rangle \rightarrow |11\rangle$, inducing gate errors, as well as control crosstalk [12]. This could be a more challenging issue when qubit frequencies are fixed [13]. Complex control pulses are proposed to resolved this issue but finding appropriate pulses remains a difficulty [12, 15]. The microwave pulses are

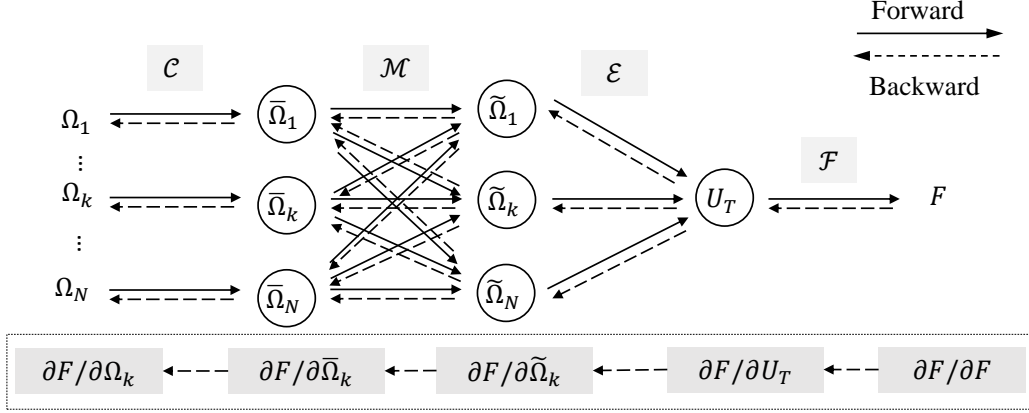


FIG. 2: Computational graph of auto-differentiation. $\mathcal{C}, \mathcal{M}, \mathcal{E}, \mathcal{F}$ denote four transform layers, corresponding to each node. $\bar{\Omega}_k, \tilde{\Omega}_k, U_T, F$ are the output sequence after each transform layer. The solid line(dashed line) is the forward propagation(backpropagation). Subscript k denotes for the index of the control sequence Ω . The dashed box at the bottom shows the process of computing the gradient of F for Ω_k , using the chain rule.

sent in to drive the transmons via this operator

$$H_d^j = a_j^\dagger e^{-i\omega_d t} + a_j e^{i\omega_d t} \quad (19)$$

where ω_d is the driving frequency. The waveform $\Omega(t)$ is applied to the drive and modulates the strength of the control pulse. Hence, the total Hamiltonian reads

$$H = H_0 + \sum_j \Omega_j(t) H_d^j \quad (20)$$

The control field could be added to both qubit 1 and 2 simultaneously or only on a single qubit 1 or 2.

To illustrate the properties of COCOA's solutions and demonstrate the advantage of the algorithm, we show some numerical examples of optimizing quantum gates in realistic system by comparing different algorithms, including COCOA, CRAB, and GRAPE. For a fair comparison, we use gradient descent optimizer Adam [76] in all these algorithms, but keep the rest steps the same as the original versions. Therefore, we denote them as COCOA, GRAPE-like and CRAB-like in our results. In the simulation, each transmon is truncated to a four-level system to better consider leakage. The model parameter we used is similar to Ref. [77] as $\omega_1/2\pi = 5.270$ GHz, $\omega_2/2\pi = 4.670$ GHz, $\alpha_1/2\pi = \alpha_2/2\pi = 220$ MHz, $g_{12}/2\pi = 25.4$ MHz. The initial pulses for all algorithms are identical and take the form as shown in Eq. (14).

Note that the coupling strength between the two qubit is at the order of $g/\omega \simeq 10^{-2}$. The results for the weak coupling $g/\omega \leq 10^{-3}$ and ultra-strong coupling regime $g/\omega \geq 10^{-1}$ are shown in appendix B, all of which demonstrating the enhancement of COCOA in the search of optimal pulses.

1. Single qubit X gate at the presence of interaction

The first gate is a single X rotation only on the second qubit while remaining the state in the first qubit. The target evolution operator of the two qubit system is

$$U_{tar} = I \otimes \sigma_x \quad (21)$$

which include both qubit's dynamics in the computational subspace $span\{|\widetilde{00}\rangle, |\widetilde{01}\rangle, |\widetilde{10}\rangle, |\widetilde{11}\rangle\}$. The identity I in the first qubit's subsystem meets the requirement that the control field does net-zero operation to the first qubit at the presence of crosstalk due to the coupling. Applying simple pulses results in entanglement between this two qubits. However, COCOA can efficiently find composite pulses to achieve the U_{tar} evolution. Here we set ω_d in resonance with transition $|\widetilde{00}\rangle \rightarrow |\widetilde{01}\rangle$, then it is off-resonant with $|\widetilde{10}\rangle \rightarrow |\widetilde{11}\rangle$ [12]. Other relevant parameters are $T = 50$ ns, $N = 148$, $f_s/2\pi = N/T = 2.96$ GHz, $N_c = 5$. The range of pulse amplitude is $[-30, 30]$ MHz $\times 2\pi$.

We can conclude three advantages of COCOA according the comparison result in Fig. 3: (1) Accuracy. As shown in Fig. 3 (a), COCOA achieves the gate infidelity below 10^{-4} , which is the same order of magnitude with GRAPE-like's result and better than CRAB-like's. Even better results could be obtained by enlarging N_c , as illustrated later in IV A 3. (2) Smoothness and bandwidth. As shown in Fig. 3 (b), the optimal pulse obtained by COCOA shows the best smoothness and limited pulse amplitude within $[-20, 20]$ MHz $\times 2\pi$. From the frequency spectrum of optimized pulse, as shown in Fig. 3 (c), COCOA has limited bandwidth but the other's consist of high-frequency components. Interestingly, GRAPE-like's pulse shows a similar profile as COCOA, with more high frequency components. Although

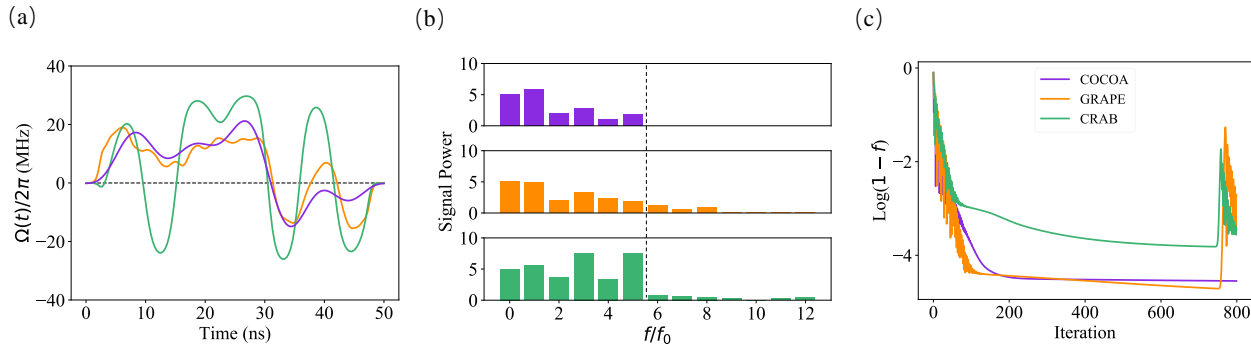


FIG. 3: Algorithm comparison.(a) Optimized pulse with zero-point at $t = 0$ ns and $t = 50$ ns. Pulse amplitude is limited between $[-30, 30]$ MHz. (b) Frequency spectrum of each pulse. $f_0 = 1/T = 0.02$ GHz. As we can see that GRAPE(orange line) and CRAB(green line) have more high-frequency components induced by pulse constraints. The dashed line shows the truncated components of the COCOA algorithm. (c) Gate infidelity changing versus iteration, showing the efficiency of each algorithm.

CRAB-like's pulse looks smooth too, its amplitude is significantly stronger than the other two. (3) Analyticity. As promised, COCOA gives a definite analytical summation form of the basis, all the high frequency components are filtered completely. Specifically, COCOA outputs the pulse parameters for Eq. (14) with

$$\begin{aligned} a_0 &= 5.066 \\ A_1, \dots, A_5 &= -11.66, -4.172, -5.753, 2.140, 3.497 \\ \phi_1, \dots, \phi_5 &= 1.080, -3.385, 6.104, -1.458, 1.098 \end{aligned}$$

GRAPE-like and CRAB-like both produce uncontrollable high frequency components and cannot obtain definite analytical expressions due to the ZERO starting and ending point constraint.

COCOA shows a great advantage here. Because the smoothness of control pulse is rather important in many qubit systems where leakage and crosstalk errors are significant. Limiting the bandwidth could also help reduce pulse distortion throughout all the control steps. Moreover, the analytical expression with definite summation of few chopped basis brings convenience and simplicity to the experimental adjustments. It is necessary to point out that, in principle, CRAB also uses analytical waveform with definite summation of chopped random basis, but the pulse constrains during optimization process induces numerical pulse distortion from the original analytical form, leading to higher frequency components, as shown in Fig. 3(c). Compared to GRAPE and CRAB, COCOA is so far the first algorithm producing definite analytical pulses.

2. Dual X gate at the presence of interaction

Simultaneously driving coupled qubits is challenging task even in tunable qubit system where the interaction

could be tuned on and off approximately. Crosstalk of control signals and zz-interaction cause significant drop of gate error compared to individual driving case. In order to implement a high fidelity dual (simultaneous) X gate on both nearest-coupled coupled qubits, we apply COCOA to find the pulses to drive them at the same time. The Dual X gate simultaneously flip the states of the first and second qubits. The target evolution operator of the two qubit system is

$$U_{tar} = \sigma_x \otimes \sigma_x \quad (22)$$

Both qubits should be driven simultaneously and the drive term follows the same form of Eq. 19. Hence, the total Hamiltonian reads

$$H = H_0 + \Omega_1(t)H_d^1 + \Omega_2(t)H_d^2 \quad (23)$$

Here we use COCOA algorithm to find the optimized driving pulse of dual X gate and we set $T = 50$ ns, $N = 200$, $N_c = 5$, $f_s = N/T = 4$ GHz. As we can see in Fig. 4, the optimized gate fidelity is greater than 99.9% and the pulse parameter for each drive are given as following:

Pulse parameters for Q1:

$$\begin{aligned} a_0 &= 5.091 \\ A_1, \dots, A_5 &= -10.46, 2.971, 3.033, 6.725, -6.124, \\ \phi_1, \dots, \phi_5 &= 5.858, 1.547, 3.085, 1.458, -3.650 \end{aligned}$$

Pulse parameter for Q2:

$$\begin{aligned} a_0 &= 5.078 \\ A_1, \dots, A_5 &= 7.790, 0.8855, 4.857, -6.030, 1.787 \\ \phi_1, \dots, \phi_5 &= 0.7156, 1.714, 2.507, 0.8538, 2.292 \end{aligned}$$

By analyzing the driving pulse and its corresponding Bloch trajectory, we found that the negative part of the driving pulse eliminates the detuning of the off-resonance subspace with respect to on-resonance subspace, namely the zz-coupling.

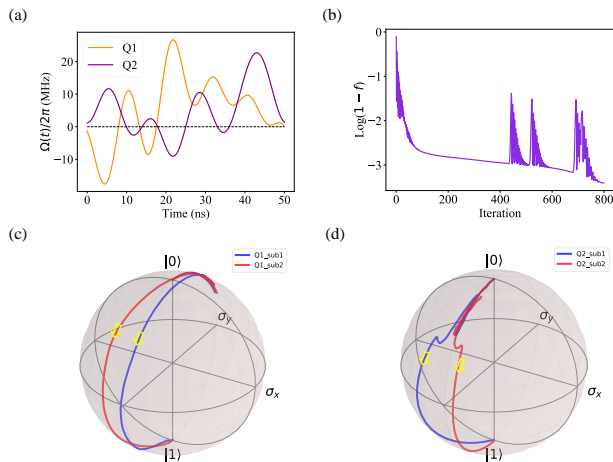


FIG. 4: Dual X gate optimization using COCOA. (a) Optimized control pulse for each qubit with pulse amplitude limitation $[-30, 30]$ MHz and ZERO starting and ending point. (b) Gate infidelity changes versus iteration, indicating the efficiency of the algorithm. (c) Evolution trajectories of qubit 1, driven by the darkorange pulse in (b). Blue(red) line shows the evolution in on-resonant (off-resonant) subspace span $\{|00\rangle, |01\rangle\}$ ($\{|10\rangle, |11\rangle\}$). (d) Evolution trajectories of qubit 2, driven by the purple pulse in (b). Blue and red line have the same meaning in (c)

3. Optimizing N_c

The key parameter N_c , i.e. the number of Fourier components, determines the smoothness and bandwidth of the pulse, as well as the number of optimizing parameters, which increases at a scaling rate of $2N_c$. Consequently, the choice of N_c affects the optimization efficiency and accuracy.

We take the previous case in Sec. IV A 1 as an example to study how N_c affects the optimization, where we only tune N_c while fixing all the other parameters. As shown in Fig. 5 (a), gate infidelity is improved by one order of magnitude when N_c increases from 1 to 5, and doesn't get much improved beyond 5. Fig. 5 (b) and (c) demonstrate the convergence behavior and pulse shape of $N_c = 1, 2, \dots, 8$. From these simulation results, we make an observation that $N_c = 5$ is the best choice based on the consideration of the trade-off between number of parameters and optimization accuracy.

Theoretically, if there is no bandwidth limit, the COCOA algorithm can approach to GRAPE algorithm when N_c reaches its maximum: $N_c^{max} = \text{Int}(\frac{N-1}{2})$, where $\text{Int}(\cdot)$ means rounding down.

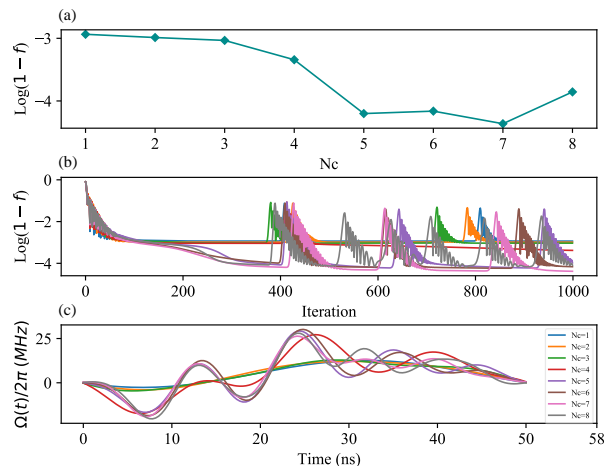


FIG. 5: Explore how N_c affects the accuracy, efficiency, and smoothness of our algorithm. (a) Best infidelity that COCOA can reach with each N_c . (b) Infidelity changes versus iterations for different N_c , indicating the efficiency. (c) Optimized pulse under different N_c .

B. Model 2: Two transmon qubits coupled via a Cavity

In another widely used architecture, superconducting qubits are coupled via superconducting cavities, such as one dimensional transmission line resonators [78–80], with the Hamiltonian

$$H_0 = \sum_{j=1,2} \omega_j a_j^\dagger a_j + \frac{\alpha_j}{2} a_j^\dagger a_j^\dagger a_j a_j + g_{cj} (b^\dagger a_j + b a_j^\dagger) + \omega_c b^\dagger b \quad (24)$$

where ω_c are the frequency of the cavity. g_{cj} is coupling strength between resonator and the j -th qubit. $b(b^\dagger)$ is annihilation(creation) operator of resonator. Other parameters have the same meaning as in model 1. We take $\omega_1/2\pi = 6.2\text{GHz}$, $\omega_2/2\pi = 6.8\text{GHz}$, $\omega_c/2\pi = 7.15\text{GHz}$, $\alpha_{1,2}/2\pi = 350\text{MHz}$, $g_{1,2}/2\pi = 250\text{MHz}$, which are used in Ref. [81]. The drive Hamiltonian H_d has the same form as Eq. 19.

Since the cavity behaves as merely a larger scale fixed-coupler between two qubits, control pulses for single-qubit gates could be obtained similarly as previous discussion. Detailed numerical results of single qubit X gate could be found in appendix C. Here we demonstrate an optimization of two-qubit entangling gate for this model.

1. Optimizing CNOT gate based on SWIPHT protocol

It's worth to point out that COCOA can fully utilize the prior knowledge of analytical methods and obtains completely analytical optimal pulses via local optimization around an analytically-given pulse. To demonstrate this, we start from a CNOT gate implementation using SWIPHT protocol (speeding up wave forms by inducing

phases to harmful transitions) [9, 10, 13, 81]. The given analytical form of the pulse is

$$\Omega(t) = \frac{\ddot{\chi}}{2\sqrt{\frac{\delta^2}{4} - \dot{\chi}^2}} - \sqrt{\frac{\delta^2}{4} - \dot{\chi}^2} \cot(2\chi) \quad (25)$$

where $\chi(t) = \frac{A}{T^8} t^4 (T-t)^4 + \frac{\pi}{4}$, $A = 138.9$, $T = 5.87/|\delta|$. $\delta = \omega_{\widetilde{10} \rightarrow \widetilde{11}} - \omega_{\widetilde{00} \rightarrow \widetilde{01}}$ is the detuning between the target and harmful transition in the computational subspace $\text{span}\{|\widetilde{01}\rangle, |\widetilde{01}\rangle, |\widetilde{10}\rangle, |\widetilde{11}\rangle\}$, where the first qubit is the control qubit and the second one is the target qubit.

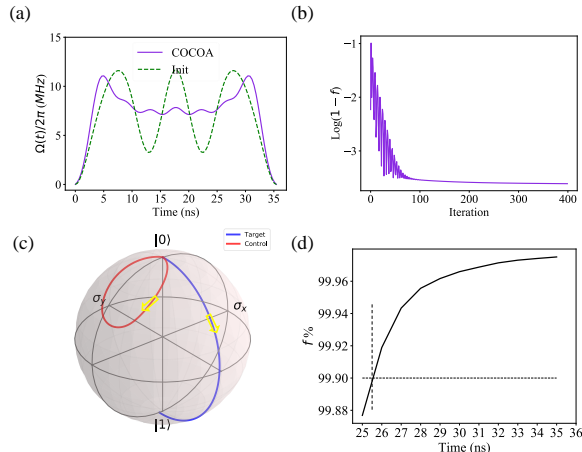


FIG. 6: CNOT gate optimization using COCOA. (a) Pulse comparison between the initial SWIFT CNOT pulse (green-dashed line) in Ref. [81] and our optimized CNOT pulse (purple-solid line). (b) Gate infidelity changes versus iteration, indicating the efficiency of the algorithm. (c) Evolution trajectory on Bloch sphere driven by our optimized pulse in (b). The blue and red lines show the target qubit’s evolution trajectory in the two subspaces $\text{span}\{|\widetilde{00}\rangle, |\widetilde{01}\rangle\}$ and $\text{span}\{|\widetilde{10}\rangle, |\widetilde{11}\rangle\}$. (d) The gate speed limit of CNOT.

The CNOT operator generated with a single microwave control could be expressed as this general form

$$U_{\text{tar}} = (\sigma_x \oplus I) \prod_{i=1,2;j=x,y,z} R_{ij}(\theta_{ij}) \quad (26)$$

where $R_{ij}(\theta_{ij})$ are single qubit rotations with arbitrary angles for optimization. This U_{tar} is equivalent to a standard CNOT $\sigma_x \oplus I$ up to some local phases. We set drive frequency $\omega_d = \omega_{\widetilde{00} \rightarrow \widetilde{01}}$, and $N_c = 9$. Fig. 6 (a) shows that the local optimization converges very fast with prior knowledge of optimal pulse, which demonstrates the advantage of numerical optimization based on analytically-optimal pulses. Fig. 6 (b) shows that the optimized CNOT pulses is transformed but still maintains similar shape as the initial analytically-optimal pulse. We note that the optimized pulse, show in Fig. 6 (b), can be generated more accurately with AWG device due to its limited bandwidth that the initial pulse doesn’t possess.

With the same evolution time $T = 35.4$ ns, we finally obtained the optimized driving pulse shown in Fig. 6 (b) with complete pulse parameters (in the unit of MHz) in Eq. 14

$$\begin{aligned} a_0 &= 7.416 \\ A_1, \dots, A_9 &= -0.818, -2.05, -2.27, -1.50 - 0.807, \\ &\quad -0.2020.0287, 0.325, 0.00291 \\ \phi_1, \dots, \phi_9 &= 0, \pi, \pi, 0, 0, 0, 0.000138, 0, 0.00198 \end{aligned}$$

The speed of this analytical CNOT gate is limited by $\frac{\delta^2}{4} - \dot{\chi}^2 > 0$ derived from Eq. 25. Hence, $T > 0.02975 \frac{A}{\delta}$, and we have $T_{\text{min}} = 24.95$ ns when $A = 138$ and $\delta = 26.4$ MHz $\times 2\pi$. The behavior of the optimal CNOT gate approaching the speed limit is shown in Fig. 6 (c). Here, we start from $T = 25$ ns and increase by 1 ns each step to observe the change of the optimal fidelity with the gate time. Finally, we obtain the gate fidelity exceeds 99.9% when $T \geq 26$ ns, which is a significantly improvement from the initial CNOT gate time 35 ns using SWIFT theory. Here we note two important tricks when using COCOA for a local optimization: 1. To obtain fast convergence in this local optimization scenario, see Fig. 6 (a), a small learning rate is favored, which is taken to be 0.001; 2. The SGD optimizer is preferred to Adam optimizer, since Adam is more suitable for broader search range due to its momentum factor [76].

V. CONCLUSION

In this paper, we have developed a novel algorithm to optimize smooth quantum control pulses constraints, which could be very complex, highly nonlinear, sub/super-differentiable approximations and optional. In the particular demonstration examples, we limit the pulse amplitude, pulse bandwidth, and the number of pulse parameters. Doing so makes this algorithm involve complicated computation for the differentiation of expectation function versus optimizing parameters. We resolve this issue using auto-differentiation powered by TensorFlow. Therefore, this algorithm can be straightforwardly extended to larger quantum systems with even more complicated calculations of gradients. We have demonstrated the advantages of the proposed algorithm by applying it to realistic superconducting qubit models with always-on ZZ-interaction, and achieve optimal smooth pulses to implement single-qubit gates and two-qubit gates. Comparing to GRAPE and CRAB algorithms, we obtain higher gate fidelities and better optimization efficiency. We have shown that COCOA could be applied to the optimization scenarios either with or without good prior knowledge by simply switching the optimizers, and obtain high-fidelity gates for both cases.

We summarize COCOA’s advantages as follows: 1. COCOA outputs optimal pulses with definite analytical expression. 2. The optimal pulses have manually limited bandwidth and amplitude. 3. This algorithm is more

compatible with complex and flexible pulse constraints, without the induced pulse distortion in numerical optimization. 4. The auto-differentiation assisted by Tensorflow enables efficient and easy calculation of gradients and the ability to handle complex computing processes and complex models. 5. COCOA can speed up the optimization by locally searching the optimal pulses based on certain prior knowledge. Using COCOA, we completely resolve the challenging problem, to implement either individually or simultaneously a single qubit X-gate in a strongly ZZ-interacting two-qubit system [12, 13, 69]. In conclusion, COCOA optimization is friendly to realistic quantum control tasks, easy to be customized, and easy to be extended to larger quantum systems.

In conclusion, COCOA provides a versatile, highly functional and efficient platform to add physical constraints into quantum optimal control tasks. Following the line of COCOA, more work could be pursued in a near future to resolve the realistic QOC issues. For example, pulse pre-distortion could be effectively performed by adding the definite transfer function of control lines and pulse generators into optimization process; Different analytical forms with fewer pulse parameters could be investigated using the proposed algorithm, so that the numerical approach could better meet the experimental needs.

Acknowledgments

This work was supported by the Key-Area Research and Development Program of Guang-Dong Province (Grant No. 2018B030326001), the National Natural Science Foundation of China (U1801661), the Guangdong Innovative and Entrepreneurial Research Team Program (2016ZT06D348), the Guangdong Provincial Key Laboratory (Grant No.2019B121203002), the Natural Science Foundation of Guangdong Province (2017B030308003), and the Science, Technology and Innovation Commission of Shenzhen Municipality (JCYJ20170412152620376, KYTDPT20181011104202253), and the NSF of Beijing (Grants No. Z190012), Shenzhen Science and Technology Program (KQTD20200820113010023).

Author contributions

YS and XHD conceived the project, designed the algorithm, performed calculations, and wrote the manuscript. YS did all the coding. JL gave some important suggestions on the algorithm and help design the flowchart. YJH helped with refining the algorithm. QG assisted with GRAPE optimization. XHD oversaw the project.

Appendix A: Low Pass Filtering

DFT: Given a discretized pulse sequence in time domain $\Omega_j[k]$, $k = 1 \dots N$. Note that the pulse here can be any form or without any form. After DFT we can get a complex sequence which contains amplitude and phase information.

$$X[n] = \sum_{k=1}^N \Omega_j[k] e^{i(2\pi n/N)k}. \quad (\text{A1})$$

We can deduce that

$$X[N-n] = \sum_{k=1}^N \Omega_j[k] e^{-j(2\pi/N)(N-n)k} \quad (\text{A2})$$

$$= \sum_{k=1}^N \Omega_j[k] e^{j(-2k\pi + (2\pi/N)kn)} \quad (\text{A3})$$

$$= \sum_{k=1}^N \Omega_j[k] e^{j((2\pi/N)kn)} \quad (\text{A4})$$

$$= X^*[n]. \quad (\text{A5})$$

This is an important characteristic of the complex sequence.

IDFT:

$$\tilde{\Omega}_j[k] = \frac{1}{N} \sum_{n=1}^N Y[n] e^{i(2\pi k/N)n}. \quad (\text{A6})$$

Assuming N is even number, We can deduce that

$$\begin{aligned} N \times \Omega_j[k] &= \sum_{n=1}^N X[n] e^{j(2\pi/N)kn} \quad (\text{A7}) \\ &= X[0] + X[1]e^{j(2n\pi/N)} + X[2]e^{j(2(2n\pi/N))} + \dots \\ &\quad + X[N/2-1]e^{j(\frac{2n\pi}{N}(N/2-1))} + X[N/2] \\ &\quad + X[N/2+1]e^{j(\frac{2n\pi}{N}(N/2+1))} + \dots \\ &\quad + X[N-2]e^{j(\frac{2n\pi}{N}(N-2))} + X[N-1]e^{j(\frac{2n\pi}{N}(N-1))}. \end{aligned} \quad (\text{A8})$$

We set $X[n] = a_n + ib_n$. Considering sum of term $X[n]$ and $X[N-n]$, by utilizing the conjugate property, we can deduce

$$\begin{aligned} (a_n + jb_n) e^{j(2\pi/N)kn} + (a_n - jb_n) e^{j(2\pi/N)(N-k)n} \\ = A_n \cos\left(\frac{2kn\pi}{N} + \phi_n\right) \end{aligned} \quad (\text{A9})$$

where $A_n = 2\sqrt{a_n^2 + b_n^2}$ and $\tan(\phi_n) = \frac{b_n}{a_n}$. Then the total expression of $\Omega_j[k]$ in time domain reads

$$\begin{aligned} N \times \Omega_j[k] &= a_0 + A_1 \cos(n2\pi/N + \phi_1) \\ &\quad + A_2 \cos((2n)2\pi/N + \phi_2) + \dots \\ &\quad + A_{\frac{N}{2}-1} \cos\left(\left((N/2-1)n\right)2\pi/N + \phi_{\frac{N}{2}-1}\right). \end{aligned} \quad (\text{A10})$$

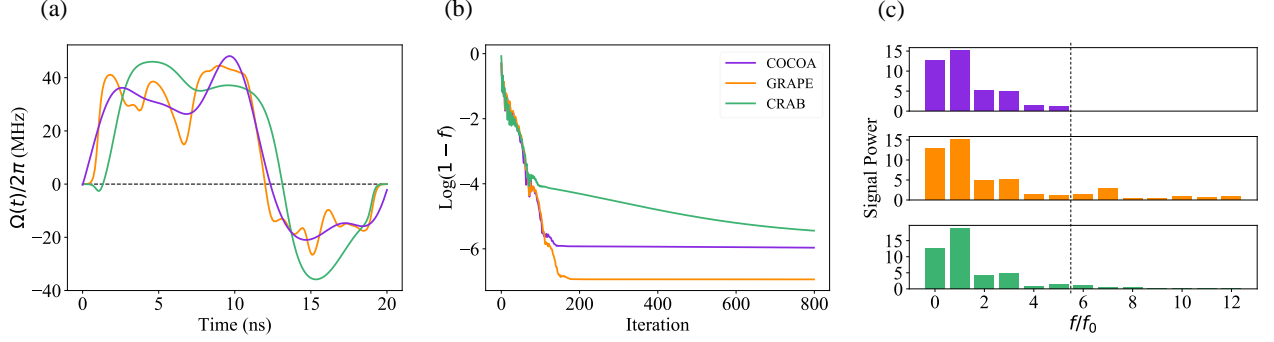


FIG. 7: Algorithm comparison. $g = 1\text{MHz} \times 2\pi$. (a) Optimized pulse with zero-point at $t = 0$ ns and $t = 20$ ns. Pulse amplitude is limited between $[-40, 40]$ MHz. (b) Gate infidelity changing versus iteration, showing the efficiency of each algorithm. (c) Frequency spectrum of each pulse. $f_0 = 1/T = 0.05$ GHz. As we can see that GRAPE(orange line) and CRAB(green line) have more high-frequency components induced by pulse constraints. The dashed line shows the truncated components of COCOA algorithm.

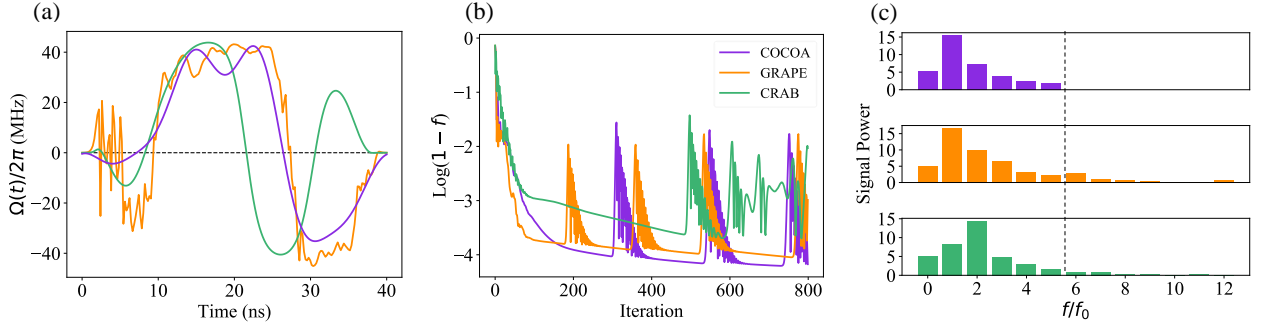


FIG. 8: Algorithm comparison. $g = 100\text{MHz} \times 2\pi$ (a) Optimized pulse with zero-point at $t = 0$ ns and $t = 20$ ns. The pulse amplitude is limited between $[-40, 40]$ MHz. (b) Gate infidelity changing versus iteration, showing the efficiency of each algorithm. (c) Frequency spectrum of each pulse. $f_0 = 1/T = 0.025$ GHz. As we can see that GRAPE (orange line) and CRAB (green line) have more high-frequency components induced by pulse constraints. The dashed line shows the truncated components of COCOA algorithm.

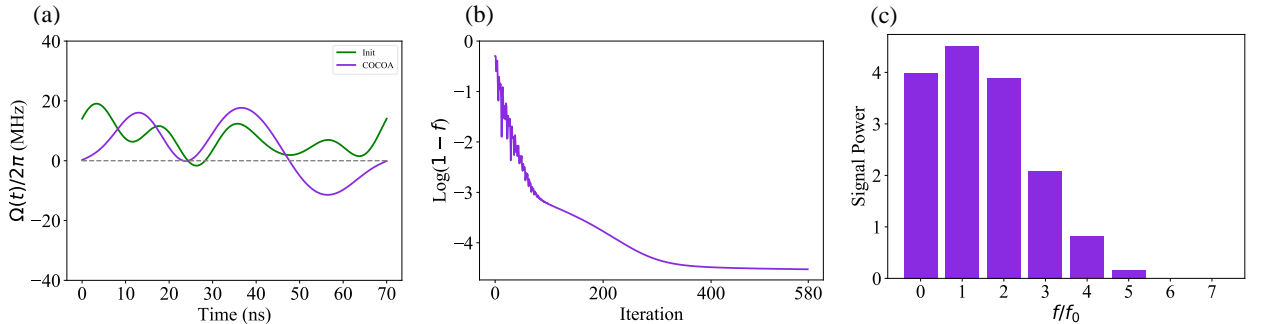


FIG. 9: Single X gate for model 2. (a) Optimized pulse with zero-point at $t = 0$ ns and $t = 70$ ns. Pulse amplitude is limited between $[-20, 20]$ (unit:MHz). The purple line is the optimized pulse with COCOA algorithm and the green line is the initial Fourier pulse. (b) Gate infidelity changing versus iteration, showing the efficiency of the algorithm. (c) Frequency spectrum of COCOA pulse with limited-bandwidth($N_c = 5$). $f_0 = 1/T = 0.0143\text{GHz}$.

Assume sample frequency is f_s we have

$$\Omega_j[k] = \Omega_j[kT_s] = \Omega_j(k/f_s). \quad (\text{A11})$$

Replace k with $f_s t$

$$\begin{aligned} N \times \Omega_j(t) &= a_0 + A_1 \cos(f_s 2\pi t/N + \phi_1) \\ &+ A_2 \cos((2f_s)2\pi t/N + \phi_2) + \dots \\ &+ A_{\frac{N}{2}-1} \cos\left(\left(\left(\frac{N}{2}-1\right)f_s\right)2\pi t/N + \phi_{\frac{N}{2}-1}\right). \end{aligned} \quad (\text{A12})$$

And we can deduce the frequency at k_c is $2\pi k_c f_s/N = 2\pi f$.

Appendix B: Weak and strong coupling strength

This appendix demonstrates that COCOA algorithm can still be efficient in different coupling strength. In

Fig. 7, we show the algorithm comparison with $g = 0.001\text{GHz} \times 2\pi$. Fig. 8 shows the result of $g = 0.1\text{GHz} \times 2\pi$

Appendix C: single qubit X gate with always on interaction for Model 2

Here we show the result of single qubit X gate in Model 2 using COCOA algorithm to show its power and compatibility to multi-qubit system. The result is show in Fig. 9.

-
- [1] A. Steane, Reports on Progress in Physics **61**, 117 (1998).
 [2] C. L. Degen, F. Reinhard, and P. Cappellaro, Reviews of modern physics **89**, 035002 (2017).
 [3] V. Giovannetti, S. Lloyd, and L. Maccone, Nature photonics **5**, 222 (2011).
 [4] T. Naranjo, K. M. Lemishko, S. de Lorenzo, Á. Somoza, F. Ritort, E. M. Pérez, and B. Ibarra, Nature communications **9**, 1 (2018).
 [5] F. B. Basset, F. Salusti, L. Schweickert, M. B. Rota, D. Tedeschi, S. C. da Silva, E. Roccia, V. Zwiller, K. D. Jöns, A. Rastelli, et al., npj Quantum Information **7**, 1 (2021).
 [6] P. Rembold, N. Oshnik, M. M. Müller, S. Montangero, T. Calarco, and E. Neu, AVS Quantum Science **2**, 024701 (2020).
 [7] Z. Chen, K. J. Satzinger, J. Atalaya, A. N. Korotkov, A. Dunsworth, D. Sank, C. Quintana, M. McEwen, R. Barends, P. V. Klimov, et al., arXiv preprint arXiv:2102.06132 (2021).
 [8] F. Motzoi, J. M. Gambetta, P. Rebentrost, and F. K. Wilhelm, Physical review letters **103**, 110501 (2009).
 [9] S. E. Economou and E. Barnes, Physical Review B **91**, 161405 (2015).
 [10] X.-H. Deng, E. Barnes, and S. E. Economou, Physical Review B **96**, 035441 (2017).
 [11] P. Doria, T. Calarco, and S. Montangero, Physical review letters **106**, 190501 (2011).
 [12] X.-H. Deng, Y.-J. Hai, J.-N. Li, and Y. Song, arXiv preprint arXiv:2103.08169 (2021).
 [13] J. Long, T. Zhao, M. Bal, R. Zhao, G. S. Barron, H.-s. Ku, J. A. Howard, X. Wu, C. R. H. McRae, X.-H. Deng, et al., arXiv preprint arXiv:2103.12305 (2021).
 [14] S. Machnes, E. Assémat, D. Tannor, and F. K. Wilhelm, Physical review letters **120**, 150401 (2018).
 [15] N. Khaneja, T. Reiss, C. Kehlet, T. Schulte-Herbrüggen, and S. J. Glaser, Journal of magnetic resonance **172**, 296 (2005).
 [16] S. Machnes, U. Sander, S. J. Glaser, P. de Fouquieres, A. Gruslys, S. Schirmer, and T. Schulte-Herbrüggen, Physical Review A **84**, 022305 (2011).
 [17] A. Ruschhaupt, X. Chen, D. Alonso, and J. Muga, New Journal of Physics **14**, 093040 (2012).
 [18] E. Zahedinejad, S. Schirmer, and B. C. Sanders, Physical Review A **90**, 032310 (2014).
 [19] T. Caneva, T. Calarco, and S. Montangero, Physical Review A **84**, 022326 (2011).
 [20] Y. Ohtsuki, G. Turinici, and H. Rabitz, The Journal of chemical physics **120**, 5509 (2004).
 [21] S. Lloyd and S. Montangero, Physical review letters **113**, 010502 (2014).
 [22] Y. Ohtsuki and K. Nakagami, Physical Review A **77**, 033414 (2008).
 [23] K. Sundermann and R. de Vivie-Riedle, The Journal of chemical physics **110**, 1896 (1999).
 [24] M. Jerger, A. Kulikov, Z. Vasselin, and A. Fedorov, Physical review letters **123**, 150501 (2019).
 [25] I. Hincks, C. Granade, T. W. Borneman, and D. G. Cory, Physical Review Applied **4**, 024012 (2015).
 [26] M. A. Rol, L. Ciorciaro, F. K. Malinowski, B. M. Tarasinski, R. E. Sagastizabal, C. C. Bultink, Y. Salathe, N. Haandbæk, J. Sedivy, and L. DiCarlo, Applied Physics Letters **116**, 054001 (2020).
 [27] Z. Tošner, T. Vosegaard, C. Kehlet, N. Khaneja, S. J. Glaser, and N. C. Nielsen, Journal of Magnetic Resonance **197**, 120 (2009).
 [28] J. A. Jones, arXiv preprint arXiv:1011.1382 (2010).
 [29] C. Ryan, M. Laforest, and R. Laflamme, New Journal of Physics **11**, 013034 (2009).
 [30] N. C. Nielsen, C. Kehlet, S. J. Glaser, and N. Khaneja, eMagRes (2007).
 [31] R. Schutjens, F. A. Dagga, D. Egger, and F. Wilhelm, Physical Review A **88**, 052330 (2013).
 [32] A. Blais, S. M. Girvin, and W. D. Oliver, Nature Physics **16**, 247 (2020).
 [33] J. L. Allen, R. Kosut, J. Joo, P. Leek, and E. Ginossar, Physical Review A **95**, 042325 (2017).

- [34] A. Blais, J. Gambetta, A. Wallraff, D. I. Schuster, S. M. Girvin, M. H. Devoret, and R. J. Schoelkopf, *Physical Review A* **75**, 032329 (2007).
- [35] A. Blais, A. L. Grimsmo, S. Girvin, and A. Wallraff, arXiv preprint arXiv:2005.12667 (2020).
- [36] I. O. Niemeyer (2013).
- [37] Z.-H. Wang and V. Dobrovitski, *Physical Review B* **84**, 045303 (2011).
- [38] F. Platzer, F. Mintert, and A. Buchleitner, *Physical review letters* **105**, 020501 (2010).
- [39] S. van Frank, M. Bonneau, J. Schmiedmayer, S. Hild, C. Gross, M. Cheneau, I. Bloch, T. Pichler, A. Negretti, T. Calarco, et al., *Scientific reports* **6**, 1 (2016).
- [40] M. Y. Niu, S. Boixo, V. N. Smelyanskiy, and H. Neven, *npj Quantum Information* **5**, 1 (2019).
- [41] C.-C. Shu, T.-S. Ho, X. Xing, and H. Rabitz, *Physical Review A* **93**, 033417 (2016).
- [42] M. Y. Niu, S. Boixo, V. N. Smelyanskiy, and H. Neven, *npj Quantum Information* **5**, 1 (2019).
- [43] S. Kirchhoff, T. Keßler, P. J. Liebermann, E. Assémat, S. Machnes, F. Motzoi, and F. K. Wilhelm, *Physical Review A* **97**, 042348 (2018).
- [44] M. Larocca and D. Wisniacki, arXiv preprint arXiv:2010.03598 (2020).
- [45] W. N. Plick and M. Krenn, *Physical Review A* **92**, 063841 (2015).
- [46] K. W. Moore and H. Rabitz, *The Journal of chemical physics* **137**, 134113 (2012).
- [47] J. Kelly, R. Barends, B. Campbell, Y. Chen, Z. Chen, B. Chiaro, A. Dunsworth, A. G. Fowler, I.-C. Hoi, E. Jeffrey, et al., *Physical review letters* **112**, 240504 (2014).
- [48] M. Rol, F. Battistel, F. Malinowski, C. Bultink, B. Tarasinski, R. Vollmer, N. Haider, N. Muthusubramanian, A. Bruno, B. Terhal, et al., arXiv preprint arXiv:1903.02492 (2019).
- [49] M. Abadi, A. Agarwal, P. Barham, E. Brevdo, Z. Chen, C. Citro, G. S. Corrado, A. Davis, J. Dean, M. Devin, et al., arXiv preprint arXiv:1603.04467 (2016).
- [50] C.-C. Shu, T.-S. Ho, X. Xing, and H. Rabitz, *Physical Review A* **93**, 033417 (2016).
- [51] L. H. Pedersen, N. M. Møller, and K. Mølmer, *Physics Letters A* **367**, 47 (2007).
- [52] L. R. Rabiner and B. Gold, Englewood Cliffs: Prentice-Hall (1975).
- [53] Z. Chen, *Metrology of quantum control and measurement in superconducting qubits* (University of California, Santa Barbara, 2018).
- [54] J. M. Martinis and M. R. Geller, *Physical Review A* **90**, 022307 (2014).
- [55] D. d'Alessandro, *Introduction to quantum control and dynamics* (CRC press, 2007).
- [56] J. Lin, F.-T. Liang, Y. Xu, L.-H. Sun, C. Guo, S.-K. Liao, and C.-Z. Peng, arXiv preprint arXiv:1806.03660 (2018).
- [57] J. Raftery, A. Vrajitoarea, G. Zhang, Z. Leng, S. Srinivasan, and A. Houck, arXiv preprint arXiv:1703.00942 (2017).
- [58] Y. Baum, M. Amico, S. Howell, M. Hush, M. Liuzzi, P. Mundada, T. Merkh, A. R. Carvalho, and M. J. Biercuk, arXiv preprint arXiv:2105.01079 (2021).
- [59] E. R. Ziegel, *Filtering in the time and frequency domains* (1988).
- [60] A. Güneş Baydin, B. A. Pearlmutter, A. Andreyevich Radul, and J. Mark Siskind, *Journal of Machine Learning Research* **18**, 1 (2018), ISSN 15337928, 1502.05767.
- [61] P. Zhao, P. Xu, D. Lan, J. Chu, X. Tan, H. Yu, and Y. Yu, *Physical Review Letters* **125**, 200503 (2020).
- [62] J. Ku, X. Xu, M. Brink, D. C. McKay, J. B. Hertzberg, M. H. Ansari, and B. Plourde, *Physical review letters* **125**, 200504 (2020).
- [63] A. V. Khaetskii, D. Loss, and L. Glazman, *Physical review letters* **88**, 186802 (2002).
- [64] L. Jacak, P. Hawrylak, and A. Wojs, *Quantum dots* (Springer Science & Business Media, 2013).
- [65] P. Maksym and T. Chakraborty, *Physical review letters* **65**, 108 (1990).
- [66] L. M. Vandersypen and I. L. Chuang, *Reviews of modern physics* **76**, 1037 (2005).
- [67] Y. Wang, A. Kumar, T.-Y. Wu, and D. S. Weiss, *Science* **352**, 1562 (2016).
- [68] M. Sarovar, T. Proctor, K. Rudinger, K. Young, E. Nielsen, and R. Blume-Kohout, *Quantum* **4**, 321 (2020).
- [69] A. Ash-Saki, M. Alam, and S. Ghosh, *IEEE Transactions on Quantum Engineering* **1**, 1 (2020).
- [70] P. Murali, D. C. McKay, M. Martonosi, and A. Javadi-Abhari, in *Proceedings of the Twenty-Fifth International Conference on Architectural Support for Programming Languages and Operating Systems* (2020), pp. 1001–1016.
- [71] J. Kelly, Z. Chen, B. Chiaro, B. Foxen, J. Martinis, and Q. H. T. Team, in *APS March Meeting Abstracts* (2019), vol. 2019, pp. A42–002.
- [72] F. Arute, K. Arya, R. Babbush, D. Bacon, J. C. Bardin, R. Barends, R. Biswas, S. Boixo, F. G. Brandao, D. A. Buell, et al., *Nature* **574**, 505 (2019).
- [73] P. Krantz, M. Kjaergaard, F. Yan, T. P. Orlando, S. Gustavsson, and W. D. Oliver, *Applied Physics Reviews* **6**, 021318 (2019).
- [74] M. Kjaergaard, M. E. Schwartz, J. Braumüller, P. Krantz, J. I.-J. Wang, S. Gustavsson, and W. D. Oliver, *Annual Review of Condensed Matter Physics* **11**, 369 (2020).
- [75] G. Wendin, *Reports on Progress in Physics* **80**, 106001 (2017).
- [76] S. Ruder, arXiv preprint arXiv:1609.04747 (2016).
- [77] J. Qiu, Y. Zhou, C.-K. Hu, J. Yuan, L. Zhang, J. Chu, W. Huang, W. Liu, K. Luo, Z. Ni, et al., arXiv preprint arXiv:2104.02669 (2021).
- [78] J. Majer, J. Chow, J. Gambetta, J. Koch, B. Johnson, J. Schreier, L. Frunzio, D. Schuster, A. A. Houck, A. Wallraff, et al., *Nature* **449**, 443 (2007).
- [79] M. Gong, M.-C. Chen, Y. Zheng, S. Wang, C. Zha, H. Deng, Z. Yan, H. Rong, Y. Wu, S. Li, et al., *Physical review letters* **122**, 110501 (2019).
- [80] J. M. Chow, J. M. Gambetta, A. D. Corcoles, S. T. Merkel, J. A. Smolin, C. Rigetti, S. Poletto, G. A. Keefe, M. B. Rothwell, J. R. Rozen, et al., *Physical review letters* **109**, 060501 (2012).
- [81] S. E. Economou and E. Barnes, *Physical Review B* **91**, 161405(R) (2015).